Article

Intelligent Optimization of Switched Reluctance Motor Using Genetic Aggregation Response Surface and Multi-Objective Genetic Algorithm for Improved Performance

Chiweta Emmanuel Abunike [1,2,*], Ogbonnaya Inya Okoro [2] and Sumeet S. Aphale [1]

1   School of Engineering, University of Aberdeen, Aberdeen AB24 3UE, UK
2   Department of Electrical/Electronic Engineering, Michael Okpara University of Agriculture, Umudike 440101, Abia State, Nigeria
*   Correspondence: c.abunike.22@abdn.ac.uk

Abstract: In this paper, a thorough framework for multiobjective design optimization of switched reluctance motor (SRM) is proposed. Selection of stator and rotor pole embrace coefficients is an essential step in the SRM design process since it influences torque output and torque ripple in SRM. The problem of determining optimal pole embrace is formulated as a multi-objective optimization problem with the objective of optimizing average torque, efficiency and torque ripple, and response surface models were obtained based on the genetic aggregation method. The results obtained by genetic aggregation response surface (GARS) and the non-dominated genetic algorithm (NSGA-II) were validated with the finite element method (FEM) model of the initial SRM. The optimized model displayed better efficiency profile over a wide speed range. The initial and optimized models recorded maximum efficiencies of 85% and 94.05%, respectively, at 2000 rpm. The efficiency values of 93.97–94.05% were achieved for the three pareto optimal candidates. The findings indicate the viability of the suggested strategy and support the use of GARS and NSGA-II as useful methods for addressing SRM key challenges.

Keywords: efficiency; genetic aggregation response surface; genetic algorithm; pole embrace coefficients; switched reluctance motor; torque ripple

1. Introduction

High performance electric machines are central in many industrial applications such as in electric vehicles, wind energy drives, aerospace, robotics, submarines and so on [1,2]. Since torque and flux control could easily be accomplished by adjusting the armature and field currents in separately excited systems where quick response is required with high performance at very low speeds, conventional DC motors have traditionally been used in adjustable speed drive applications [3]. The disadvantage of these DC motors is the mechanical commutator assembly coupled with brushes for electrical continuity of the rotor mounted armature coil, which increases shaft inertia and slows response time [4]. Additionally, they need regular maintenance since brush wear reduces motor life and the commutator's efficiency in high-speed applications due to arcing and heating with large current carrying capacities [3,5]. Similarly, the major concern with permanent magnet synchronous generators is the high expense of the premium permanent magnets needed to make them [6,7]. The employment of non-conventional electrical machines such as switched reluctance motors (SRMs) has drawn the attention of the majority of researchers and industrialists as a means of resolving these problems [8–11].

SRMs have been used in several industrial applications such as: linear transportation [12], wind generators [13], mining equipment [14], flywheel energy storage applications [15], high speed and high power applications [16,17], different generators [18–20], automotive applications [21–23]. This is due to their simple structure, low manufacturing

cost, and high robustness. The power density, efficiency and torque output of SRMs are high over a wide speed range [24,25]. These merits have increased the research efforts and made SRMs preferred for high speed applications [10,22,25]. Several multi-objective optimizations of SRMs have been studied in [26–32] and good results were obtained. The optimization process was carried out to increase SRM's average torque and decrease its torque ripple in order to enhance the overall performance of SRMs in [28]. In [29], the optimization was performed by considering the ratio between the length of an SRM core to the pole arcs of a stator and rotor. The stator and rotor pole arcs were varied to achieve a self-starting positive torque. With every variation in stator and rotor pole arcs, the objective functions (average torque and torque per volume) were calculated. A compromise between the average torque and the torque per volume numbers led to the selection of the arc's values. However, the work assumed fixed ratios for the lengths and arcs and did not consider other values which many produce another optimal design. In [33], multi-objective optimization of SRM for electric vehicle (EV) applications was proposed. Three objective functions (torque per volume of the core of the motor, average torque per copper loss, and average torque) based on the requirements of EVs were optimised using three weight factors and three base values, while the optimised parameters were only the stator and rotor pole arcs' angles.

Recently, a new family of electric machine design optimization methods which involve stochastic evolutionary approaches and design of experiments (DoE) are noteworthy [9,34–36]. The techniques minimize the computing complexity of the conventional strategies that relate stochastic evolutionary methods with finite element analysis (FEA). The central composite design (CCD) was applied to the creation of response surface (RS) models in [35]. Based on the first-order regression coefficients of the RS models, sensitivity tests were carried out to determine the significant design variables. However, while employing the first-order regression coefficients as the sensitivity indices, the impacts of the interactions between design factors were not taken into account. Following the sensitivity analysis, the ideal values of the chosen significant design variables were determined using a differential evolutionary method in conjunction with an FEA solver. Due to the usage of the FEA for each candidate design, the optimization procedure had a significant computing cost. The high computational cost was eliminated by coupling the evolutionary method with RS models in [36]. DoE was utilised to build the second-order RS models, which were then used to forecast the machine responses throughout the optimization's search phase. The search algorithm for the best designs successfully lowered the computing cost by removing FEA iterations. However, the second-order RS model's drawback is that its accuracy declines with the size of the design space, which could result in inaccurate optimal solutions. Furthermore, more samples are needed to cover the design space with a larger dimension for the RS model's construction. The distribution of the samples is crucial to the RS model's reliability. The CCD samples, however, are proportional to the size of the design space. As a result, applying the CCD to the target problem may not be appropriate. However, the distribution of the samples obtained through the Latin Hypercube Design (LHD) method must be carefully planned in order to guarantee the accuracy of the RS model [24]. On the other hand, the quantity of samples obtained through the LHD method is controllable. Thus, the accuracy of RS models and selection of acceptable methods are the major difficulties associated with the conventional RS model-based techniques which will be addressed in this study.

To the best of the authors' knowledge, this is the first attempt to improve SRM performance by considering the effect of pole embrace (ratio of pole arc to pole pitch) of a rotor and stator, yoke thickness of a stator and saturation level in the multi-objective optimization process by using genetic aggregation response surface (GARS) and the non-dominated genetic algorithm (NSGA-II). It is clear from the analysis of the literature [9] that different optimization methodologies should be investigated in relation to the design optimization of SRM. To this end, the current study is focused on the application of GARS and MOGA in order to achieve enhanced design of SRM with increased performance. Because of its su-

perior computing complexity, guarantee of elitism, and more even individual distribution than the pareto front, NSGA-II is preferred [37].

The fundamental drawback of SRM is its doubly salient pole configuration, which results in a relatively significant torque ripple. This results in a high torque ripple, noise and vibration effects during the operation of the motor. To minimise torque ripples in SRM, two alternative strategies are taken into account which include geometry modification/optimization and deployment of control algorithms to improve the performance [25,37]. The control of SRM plays an essential role in its operation and it differs depending on the application [13,24,25]. Additionally, even when using electronic torque ripple reduction approaches, it is preferable to search the best SRM geometry for enhanced improvement [38].The stator-rotor pole overlap angle, pole shape, material attributes, number of poles, and number of phases affect the torque characteristics of SRM [7,39]. The pole arcs and tooth widths of the stator and rotor, which are influenced by the pole embrace coefficients of both the rotor and the stator, have an impact on the torque output and torque ripple of SRM. To ensure enough torque during phase commutation, the stator and rotor of the motor should be built with sufficient pole overlap. The best pole embrace arrangement must be chosen in order to minimise torque ripple because of their direct impact on inductance and torque calculation. However, proper consideration should also be paid to the stator's yoke thickness because wider stator pole causes more copper loss and availability of a smaller window for winding [40]. As a result, the problem of determining the ideal stator yoke thickness and pole embrace coefficients of the stator and rotor is formulated in this paper as a multi-objective optimization problem with the objectives of optimizing average torque, efficiency and torque ripple by seeking an optimum flux density. The maximum flux density in the motor will be limited to this optimum value. The main findings of this study will serve as an important tool for designers as it allows them to relate the effects of geometric dimensions on the motor performance.

The remainder of this paper is organized as follows. Section 2 presents the design concept and initial consideration of the proposed motor. Section 3 shows the formulation of optimization objective functions and constraints. The comprehensive framework based on GARS and MOGA for optimal design of SRM is proposed in this section. Section 4 presents the simulation results, and in Section 5, the conclusions are presented.

2. Design Concept and Initial Consideration

SRMs' designs are less complex than those of other machine designs because of their simple structure [24]. The number of salient rotor and stator poles is uneven. The stator carries the coils, while the rotor has no cage and magnets. The operation of the SRM is dependent on the fluctuating reluctance created by the air gap between the stator and the rotor. Figure 1 is the cross-sections of the geometry of the SRM while the values of various parameters are presented in Table 1.
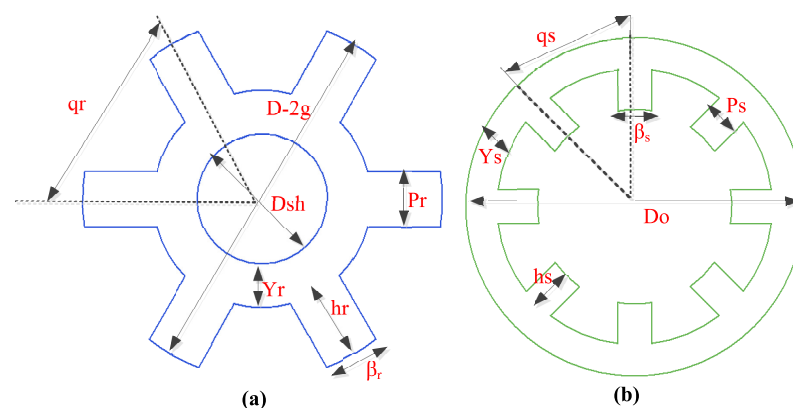
Figure 1. Geometric parameters of 8/6 SRM for (**a**) Rotor (**b**) Stator.

Table 1. Parameters of the SRM.

Parameters	Values
Rated voltage	380 V
Rated speed	1000 rpm
Power output	1.50 kW
Stacking factor	0.95
Core length	65 mm
Stator pole number	8
Stator outer diameter	120 mm
Stator inner diameter	75 mm
Stator pole embrace	0.45
Stator yoke thickness	12 mm
Rotor pole number	6
Rotor pole embrace	0.30
Rotor yoke thickness	9 mm
Rotor inner diameter	27.10 mm
Rotor outer diameter	74 mm
Ferromagnetic material	M19 steel (24 gauge)

$(D, D_{sh}, g, P_r, q_r, Y_r, h_r, \beta_r, q_s, Y_s, h_s, P_s, \beta_s, D_0)$ in Figure 1 represent bore diameter, shaft diameter, air gap length, rotor poles, rotor pole pitch, rotor yoke thickness, rotor pole length, rotor pole arc, stator pole pitch, stator yoke thickness, stator pole length, stator poles, stator pole arc, and outer diameter, respectively. Due to the effect of magnetic saturation on the flux linkage-to-angle curve, SRM is expected to be operated with a unipolar current excitation, and its mathematical model is nonlinear [24]. The phase voltage equation used to calculate the torque is given as [41]:

$$v_{ph} = R_s i_{ph} + \frac{d\lambda_{ph}\left(i_{ph}, \theta_{ph}\right)}{dt}, \tag{1}$$

$$L_T\left(i_{ph}, \theta_{ph}\right) = \frac{d\lambda_{ph}\left(i_{ph}, \theta_{ph}\right)}{di_{ph}}, \tag{2}$$

$$E_{ph} = \frac{d\lambda_{ph}}{d\theta_{ph}}\omega, \tag{3}$$

$$v_{ph} = R_s i_{ph} + L_T\left(i_{ph}, \theta_{ph}\right)\frac{di_{ph}}{dt} + E_{ph}, \tag{4}$$

$$W\left(i_{ph}, \theta_{ph}\right) = \int_0^{i_{ph}} \lambda_{ph}\left(i_{ph}, \theta_{ph}\right) di_{ph}, \tag{5}$$

$$T = \frac{\partial W\left(\theta_{ph}\right)}{\partial \theta_r}. \tag{6}$$

The equation for motion is given as:

$$J\frac{d\omega}{dt} = T - T_L - B_m\omega, \tag{7}$$

where v_{ph} stands for voltage per phase; R_s stands for stator resistance per phase; i_{ph} stands for current per phase; θ_{ph} stands for angle per phase; λ_{ph} stands for flux linkage per phase; J stands for rotor inertia; T stands for rotor torque; T_L stands for load torque; B_m stands for rotor damping; and ω stands for mechanical rotational speed.

The design procedure of SRM starts with specifying the available dimensions from space constraints such as shaft size, axial length, number of stator and rotor poles, pole arcs, pole pitch, and so on. The number of stator poles P_s and the number of rotor poles P_r are usually selected based on experience with the application requirements and converter

configuration to be used. This paper primarily focuses on the 8/6 topology because it has the advantage of lower torque ripple than the conventional 6/4 topology.

Referring to [42], the minimum stator pole arc to achieve self starting is given as:

$$\min[\beta_s] = \frac{4\pi}{P_s P_r}. \tag{8}$$

The following is the requirement that guarantees there is no overlap of the stator and rotor poles in the unaligned position:

$$\beta_s + \beta_r \leq= \frac{2\pi}{P_r}, \tag{9}$$

where β_r and β_s represent the pole arcs of the rotor and stator, respectively. The motor will develop positive inductance rate of change before reaching the minimum value if (9) is not obeyed. This will cause the unaligned inductance value to be higher which will result in lower torque generation.

The following is the stator pole arc length, t_s, at the winding's closest point to the shaft's centre:

$$t_s = (\frac{D}{2})\beta_s + 2h_{wed}, \tag{10}$$

where the wedge, h_{wed}, is chosen as 4 mm which is required to hold the windings in place as calculated in [25]. Calculating a modified stator pole pitch, q_{sb}, and incorporating the wedges holding the windings in place leads to:

$$q_{sb} = \frac{\pi(D + 2h_{wed})}{P_s}. \tag{11}$$

The maximum height of the winding (h_w) is obtained by subtracting (h_{wed}) from stator pole height (h_s):

$$h_w = h_s - h_{wed}. \tag{12}$$

The number of layers that can fit in the available winding height is calculated as follows:

$$N_v = \frac{h_w K_f}{d_w}, \tag{13}$$

where K_f represents the fill factor. The value of N_v is rounded off to the nearest lower integer while the number of horizontal layers needed for the winding is provided by:

$$N_h = \frac{T_{ph}}{N_v}. \tag{14}$$

The distance between two stator pole tips at the bore is given by:

$$Z = p_b - t_s. \tag{15}$$

The width, w_t, of the winding and the clearance, CL, between the winding at the bore are respectively given as:

$$w_t = d_w \frac{N_h}{K_f}. \tag{16}$$

$$CL = Z - 2w_t. \tag{17}$$

The magnetic flux density distribution of the SRM is displayed in Figure 2. It could be observed that the maximum flux density at the pole is higher than the knee point (1.86 T) of the core material (M19-24G). Design experience has proven that limiting the motor's

maximum flux density to this value is a recommended practise. Noise in the motor is reduced as a result of this practise [43].
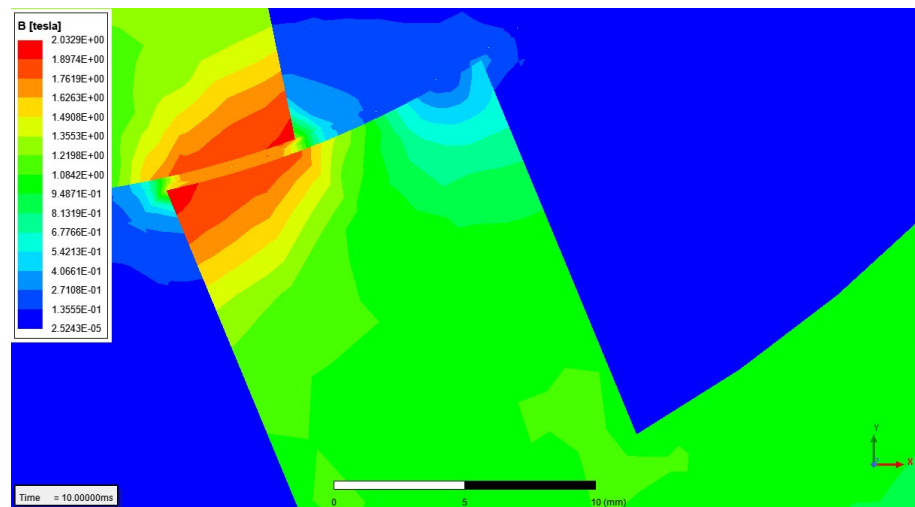
Figure 2. Magnetic flux and field distributions of the SRM model showing maximum flux density of 2.03 *T* around the poles of the motor.

The stator pole area, A_s, is defined as:

$$A_s = \frac{D}{2} L \beta_s. \tag{18}$$

The flux in the stator pole and yoke are respectively defined as:

$$\phi = B_s A_s, \tag{19}$$

$$\phi_y = \frac{\phi}{2} = \frac{B_s A_s}{2}. \tag{20}$$

If the yoke flux density, B_y, is half the stator flux density B_s, the yoke flux and flux density in the rotor pole, B_r, can respectively be written as:

$$\phi_y = B_y A_y = \frac{B_s}{2} A_y. \tag{21}$$

$$B_r = \frac{B_s A_s}{A_r}. \tag{22}$$

The area of the rotor core, A_{rc}, is given by:

$$A_{rc} = L(\frac{D}{2} - g - h_r - \frac{D_{sh}}{2}). \tag{23}$$

The reluctance, $\mathscr{R}$, of the air gap is given as:

$$\mathscr{R} = \frac{2l_g}{\mu_0 A_g}, \tag{24}$$

where μ_0 and A_g are the permeability of free space and air gap area, respectively. The air-gap flux density, B_g, and magnetic field intensity of the air-gap, H_g, are respectively given as:

$$B_g = \frac{A_s B_s}{A_g}. \tag{25}$$

$$H_g = \frac{B_g}{4\pi * 10^{-7}}. \tag{26}$$

The magnetic circuit of the SRM is shown in Figure 3. The reluctances of the stator pole, yoke, rotor pole, rotor core and air-gap are represented by $\mathcal{R}_s$, $\mathcal{R}_y$, $\mathcal{R}_r$, $\mathcal{R}_{rc}$, and $\mathcal{R}_g$, respectively.
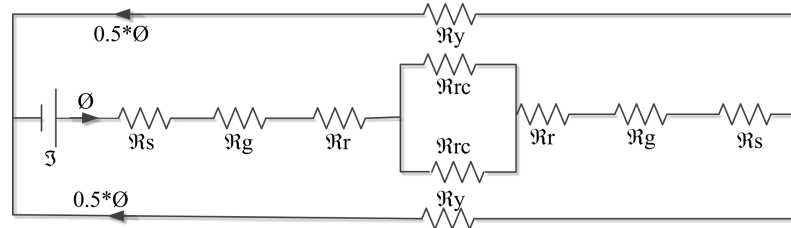
Figure 3. SRM's magnetic circuit showing the interconnection of circuit parameters.

The mathematical representation of reluctance, $\mathcal{R}$, in any section is:

$$\mathcal{R} = \frac{H * L}{B * A} = \frac{H * L}{\phi}, \tag{27}$$

where H is the magnetic field intensity, L is the section's mean path length, B is the section's flux density, A is the section's area, and ϕ is the section's flux.

The torque ripple, TR, is defined as [24]:

$$TR = \frac{T_{max} - T_{min}}{T_{avg}}, \tag{28}$$

where the maximum, minimum, and average torques are denoted by T_{max}, T_{min}, and T_{avg}, respectively.

The efficiency of SRM, η, is given as the ratio of shaft power output and motor input power, which will be computed from input current and voltage waveforms during period, T_s, in accordance with the following equation:

$$P_{in} = \frac{m}{T_s} \sum vi\Delta t, \tag{29}$$

where m is number of phases and Δt is sampling time of the current and voltage waveforms. The efficiency can also be predicted by the knowledge of losses [44–46]. Due to the non-sinusoidal nature of the flux waveforms and the variations in the shape of the flux density waveforms in different sections of the SRM's magnetic circuit, calculating losses in the SRM, and particularly assessing core losses, is a highly challenging task. Additionally, rotation speed and the type of control employed both affect core losses. For low speeds, the mechanical losses can be neglected. Hence losses, T_L, may be calculated as:

$$T_L = Copper\ Loss + Core\ Loss. \tag{30}$$

Once the losses are obtained, the efficiency is calculated as:

$$\eta = \frac{T_L T_{avg}}{T_L T_{avg} + T_L}. \tag{31}$$

3. Multi-Objective Optimization

Evolutionary algorithms are effective techniques for achieving the best possible product design. Single-objective and multi-objective optimization algorithms are the two main categories of optimization algorithms in terms of objective functions. In single-objective optimization, one objective function is present, or occasionally, the entire objective function is made up of several objective functions that have been combined into one objective

function using weighing factors. The drawback of single-objective optimization algorithms is that choosing weights does not guarantee that the eventual result will be satisfactory. Additionally, a consistent and continuous variation of the weights may not always produce an accurate and comprehensive depiction of the pareto optimal set [47].

On the other hand, multi-objective optimization allows the optimization of more than one single objective function and is based on non-dominated solutions, meaning that a function cannot be decreased without at least one other function also increasing at the same time. Objective functions in multi-objective optimization may conflict. It follows that enhancing one objective function will make the other one worse. As a result, multi-objective optimization allows the simultaneous consideration of several objectives and the existence of a set of optimal solutions, in contrast to single-objective optimization where there is only one extreme for the problem. The Pareto-front is a collection of solutions where a user must select the best option among a large number of similar options based on the demands of a particular application. Additionally, since contradictory objective functions can be included in the optimization problem, which gives a mathematically precise definition of compromise solution, multi-objective optimization eliminates the challenges associated with the selection of weighing factors and produces more realistic results [47,48]. To accurately complete the multi-objective goal of the studied SRM, a minimum of two factors are needed. First, the motor's mathematical model (explained in Section 2), which provides information on the SRM's efficiency, average torque and torque ripple for any set of variable parameters. The second factor, the search algorithm, operates under the multi-attribute rule [41].

3.1. Non-Dominated Sorting Genetic Algorithm II (NSGA-II)

The SRM is designed optimally in this paper using the non-dominated sorting genetic algorithm II (NSGA-II). When compared to other multi-objective approaches such as Pareto-archived evolution strategy and strength-Pareto evolutionary algorithm, this algorithm performs better in terms of finding a variety of solutions and convergent to the exact Pareto-optimal set [47,48]. The summary of NSGA-II is depicted in Figure 4.
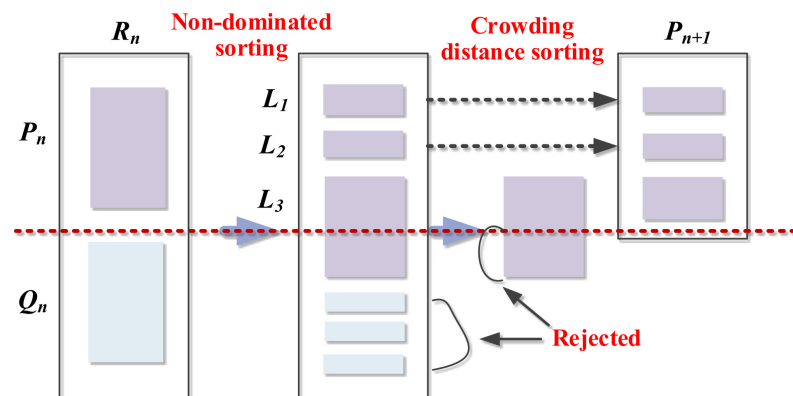

Figure 4. NSGA-II procedure for MOGA showing the different layers of the sorting process [48].

From Figure 4, the stages are as follows:

Stage 1: A parent population, P_0, of size N_p is produced. Then, a population of offspring, Q_0, is produced using the cross-over and mutation operations. In order to facilitate generalisation, subsequent phases are stated as nth generation.

Stage 2: Production of the combined population $R_n = P_n \cup Q_n$. The size of the population R_n is $2N_p$.

Stage 3: Decoding the combined population R_n and determining the fitness of the objective functions. The population R_n is then sorted using non-dominated solution sets such L_1, L_2, and L_3. The best solutions for the problem are those that belong to the best

non-dominated solution set L_1, as can be seen in Figure 4. Solutions from the set L_3 are picked last and in second priority, then solutions from the set L_2.

Stage 4: The initial sets are chosen when the total of their members equals or exceeds N_p. Every member's crowding distance inside the chosen sets is computed. For the following generation P_{n+1}, the first k_1 sets are chosen based on elitism. According to crowding distance, the kth set is sorted, and those with a high crowding distance are chosen and added to the P_{n+1} generation after them until the population reaches N_p.

Stage 5: If the number of generations reaches its limit, the programme ends and the fitness of the objective functions and non-dominated solutions are found. If not, proceed to Stage 6.

Stage 6: The new population P_{n+1} is subjected to crossover and mutation operators to produce the new population Q_{n+1}, after which Stage 2 is reached.

For any member g and h, selection in NSGA-II is based on the crowded-comparison operator provided by (32).

$$g < h, \ if \ (g_{rank} < h_{rank}) \ or \ ((g_{rank} < h_{rank} \ and \ (g_{dist} < h_{dist})), \tag{32}$$

where the non-domination ranks for the individual members of g and h are g_{rank} and h_{rank}, respectively. The crowding distances for single members of g and h are g_{dist} and h_{dist}, respectively. According to the relation $g < h$, the single member, g, is superior than the separate member, h, which means that the solution with the better (least) non-domination rank is picked. The option with a greater crowding distance is picked if the two solutions have the same ranks. The designer must classify the non-dominated solution that was obtained and choose one based on the importance of the objectives. In this paper, the order of priority is efficiency, torque ripple, and average torque.

### 3.2. Proposed Framework for Multiobjective Design Optimization of SRM

The comprehensive framework for multi-objective design optimization of the SRM is presented in this section. Table 2 displays the maximum and minimum limits of the design variables while Figure 5 is the proposed framework implemented by using ANSYS Workbench.

Table 2. Ranges of design variables.

Parameters	Range
Stator yoke thickness, Y_s	10.80–13.20 mm
Stator pole embrace, E_s	0.41–0.50
Rotor pole embrace, E_r	0.27–0.33
Stator pole flux density, B_{sp}	1.86 T
Torque ripple	20.41%
Average torque	16.32 Nm
Efficiency	85%

The proposed framework of Figure 5 begins with setting the maximum and minimum limits of the design variables as presented in Table 2. The first phase entails choosing three parameters (torque ripple, efficiency, and average torque) as the output variables, and three parameters (pole embrace of stator, pole embrace of rotor and yoke thickness of stator) as the input variables and flux density of stator pole as the seek variable. The generation of different sample points was carried out in the second step.

The central composite design approach is the DOE strategy used in this work. It establishes how many and which design points (DP) should be resolved in order to optimise as effectively as possible. There are 15 design points at which the parameters will be solved. The variations of B_{sp} with the design points are shown in Figure 6, while the relationships between the input parameters and design points are presented in Figure 7.
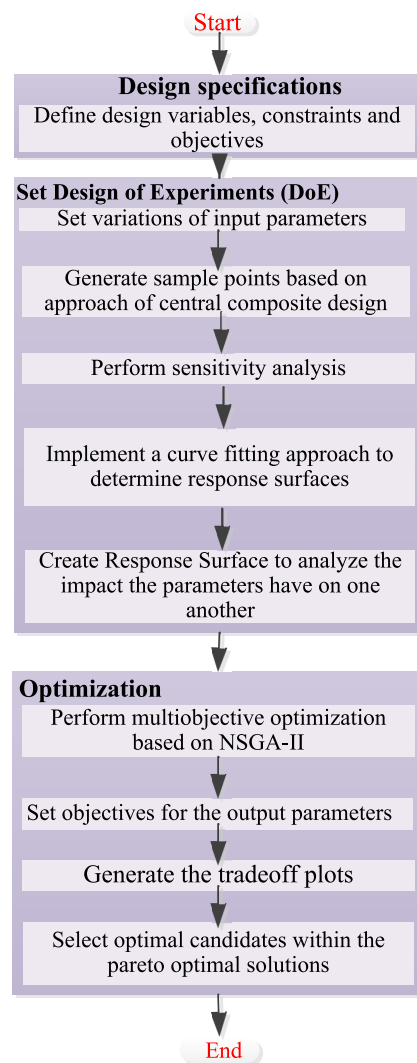
Figure 5. Illustration of the proposed scheme implemented in ANSYS workbench. As shown, the process can be broadly split into three sub-process viz: design specifications, DoE and optimization.
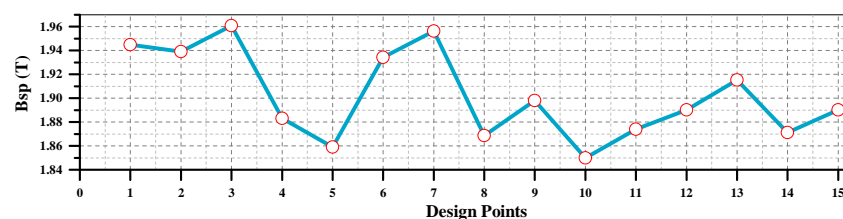
Figure 6. Target parameter of B_{sp} with design points.

From Figure 6, it can be seen that $DP - 5$ has the best 1.86 T while $DP - 10$ recorded the lowest 1.86 T. These design points do not guarantee best and worst performance. This is further shown in the plot of the output parameter relationship with the design points of Figure 8. In addition, the accurate selection of the input parameters of Figure 7 will be ascertained after investigating the optimized motor response at the target value of 1.86 T.
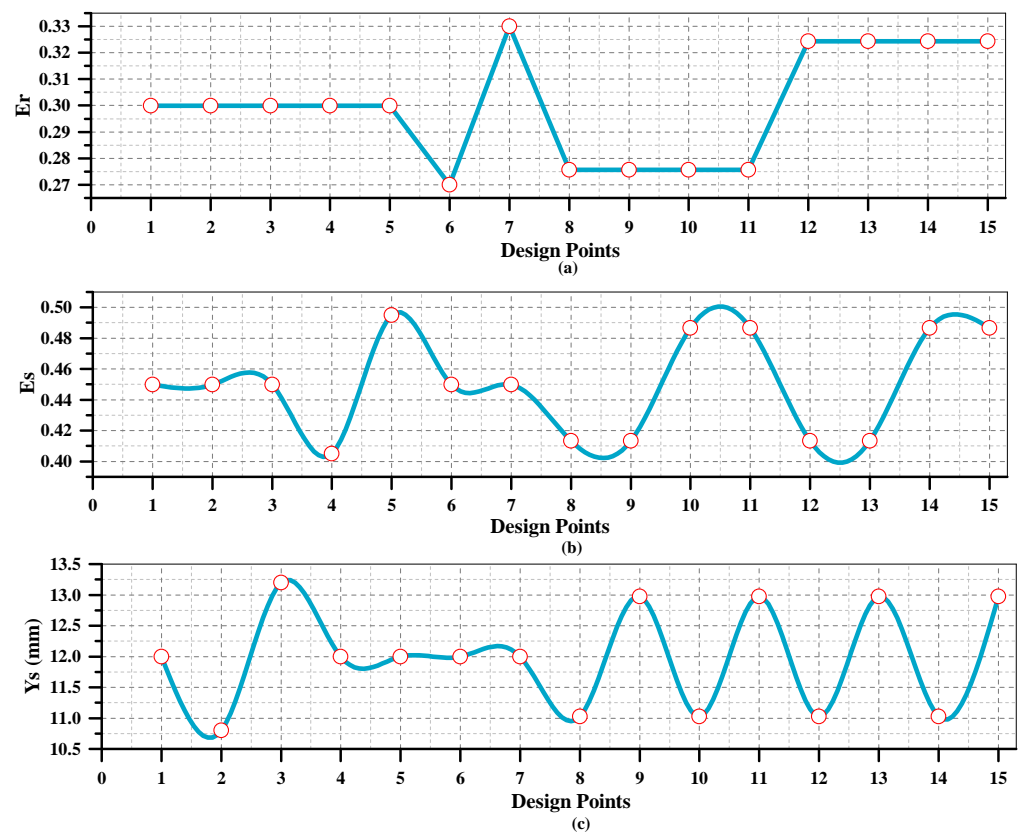
Figure 7. Input parameters with design points (**a**) E_r with design points (**b**) E_s with design points (**c**) Y_s with design points.

The motor response relationships are presented in Figure 8.

From Figure 8a, $DP-3$ and $DP-9$ gave the best efficiency, while $DP-13$ gave the best average torque in Figure 8b. In addition, $DP-15$ gave the lowest torque ripple in Figure 8c. It can be observed that none of these design points correspond to $DP-5$ of Figure 6. Hence, the DoE has fallen short of predicting the behavior between the variables. Therefore, there is need to employ a better technique in order to find the optimal combination of these variables that will give the best response at 1.86 T.

In this study, the sensitivity of the motor responses to each design feature is quantified using a genetic aggregation response surface (GARS) based sensitivity analysis approach. According to [9,35,36], local sensitivity assessments of SRM have traditionally been carried out using the one-factor-at-a-time technique. However, this approach did not take into account the interactions between the design variables or quantitatively assess the sensitivities. Due to the utilisation of numerous response surfaces and the cross-validation procedure, GARS is more reliable than the traditional response surface meta-models [49]. The functional relationship between global objective and constraint functions in a design space of response surface can be approximated as [50]:

$$y_{(x)} = \sum_{i=1}^{N_m} a_i \varphi_i(x). \tag{33}$$

The second order polynomial when solving quadratic approximation is given as:

$$1, x_1, x_2, \dots, x_n, x_1^n, x_1, x_2, \dots, x_1 x_n, \dots, x_n^2, \tag{34}$$

while the prediction of the ith response of the surrogate model is given as:

$$\hat{y} = a_0 + \sum_{i=1}^{N_m} a_i x_i + \sum_{i=1}^{N_m} a_{ii} x_i^2 + \sum_{i=1}^{N_m} a_{ij} x_i x_j. \tag{35}$$

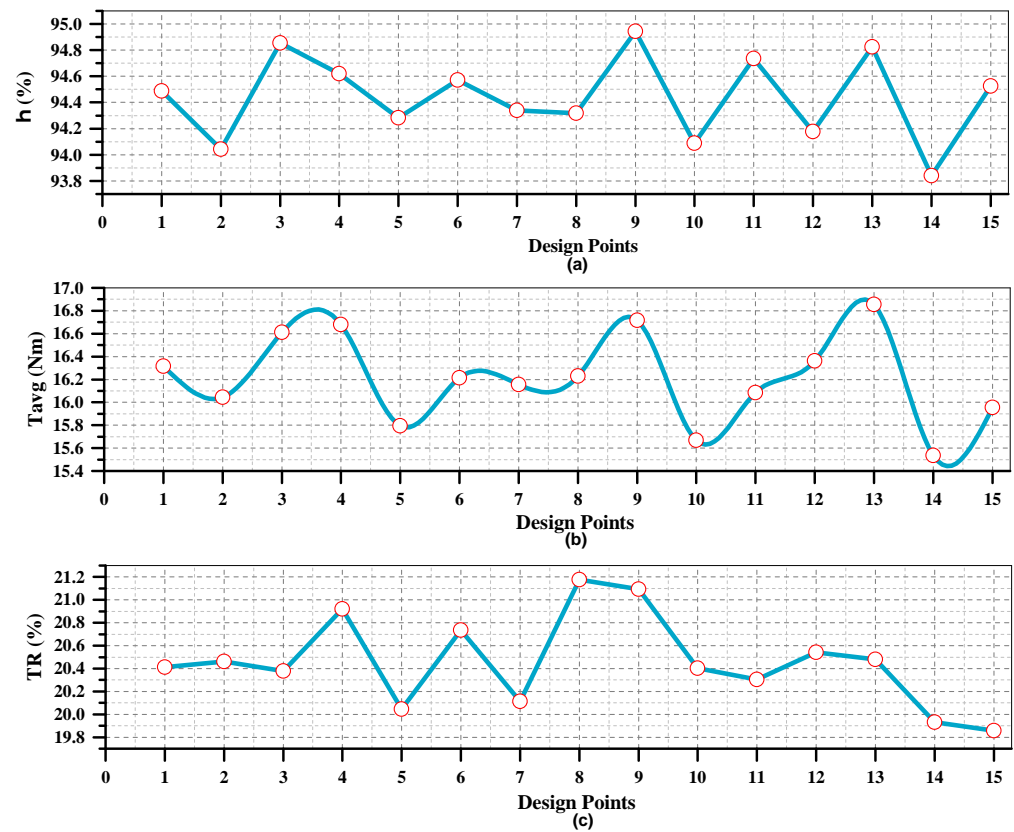It should be noted that a_i is determined by using the least squares regression given as:

$$a = (X^T X)^{-1} X^T y, \tag{36}$$

The genetic aggregation response surface adopted in this paper is expressed as an ensemble using weighted average of several different meta-models [50]:

$$c(x) = \sum_{i=1}^{N_m} w_i . \hat{y}_i, \tag{37}$$

while w_i satisfies:

$$\sum_{i=1}^{N_m} w_i = 1 \; and \; w_i \geq 0, 1 \leq i \leq N_m. \tag{38}$$


Figure 8. Output parameter with design points (**a**) η with design points (**b**) T_{avg} with design points (**c**) *TR* with design points.

The symbols used in Equations (33)–(38) are presented in Table 3.

Table 3. Symbols in Equations (33)–(38).

Symbols	Description
$y(x)$	Relation between objective and constraint functions
$\varphi_i(x)$	Basic functions
x	Design variables
a_i	Weighting parameters
N_m	Number of meta-models
$\hat{y}$	The predicted *i*th response surface
$\hat{y}$	The predicted ensemble
X	Matrix of basic functions
X^T	Transpose of the matrix of basic functions
w_i	The weight factor of the *i*th response surface

GARS creates a population of meta-models with a diverse array to maximise the likelihood of receiving the most efficient solution. This population is equivalent to the genetic algorithm's initial population. By combining prior populations and mutating them, the next populations are created. The genetic algorithm keeps other response surfaces that are less prevalent while removing a portion of the response surface type that is over represented in the population in order to maintain the diversity of response surfaces. When the anticipated values are different, the population contains similar meta-models in terms of prediction accuracy, which raises the likelihood that errors will be eliminated on the ensemble [50]. The sensitivity indices of the motor responses to the design variables are evaluated and the results are shown in Figure 9.
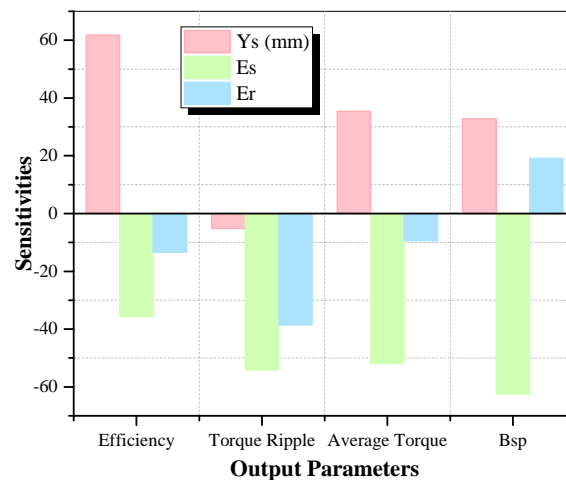
Figure 9. Sensitivity Chart. It is used to identify key variables impacting performance metrics, and the quantitative nature of their impact, respectively.

From Figure 9, the efficiency and average torque response have a positive sensitivity with stator yoke thickness, Y_s and negative sensitivity with stator pole embrace, E_s and rotor pole embrace, E_r, while the output parameter of torque ripple has a negative sensitivity with them. The set target, B_{sp} has a positive sensitivity with Y_s and E_r, and negative sensitivity with E_r. All of these sensitivity tendencies are in line with general machine design experience, and the chart can also be used to determine the important ratio.

After sensitivity analysis, the RS models are constructed by considering the data of DoE of Figures 6–8. The accuracy of the RS models highly depends on the DoE and the curve fitting approach. The accuracy of the Curve Fitting can be analyzed by using the fit accuracy approach as presented in Figure 10.
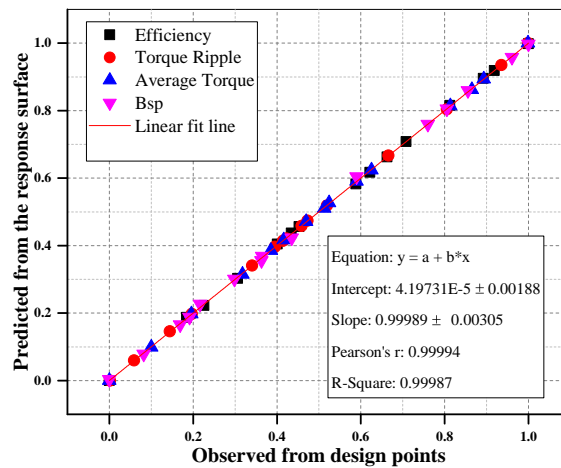
Figure 10. Fit accuracy plot showing how closely the output parameters fit the expected response.

The goodness of the line can further be examined by checking the R-squared value from Figure 10. The value gives a sense of how closely the points fit the matched line. Normally, the value should be close to 1 [51], and in Figure 10, the value is 0.99987 which is satisfactory. Based on the accuracy of the plot, the response surface analysis can accurately predict the design points.

The three-dimensional (3D) response surfaces of the motor response are presented in Figure 11. This is a useful approach used to visualize and analyze the impact that parameters have on one another. The approach assumes that all the parameters are significant by searching for higher order trends. The values of these parameters are listed in Table 4.

(**a**) B_{sp} with E_s and Y_s

(**b**) T_{avg} with E_s and Y_s

(**c**) TR with E_s and Y_s

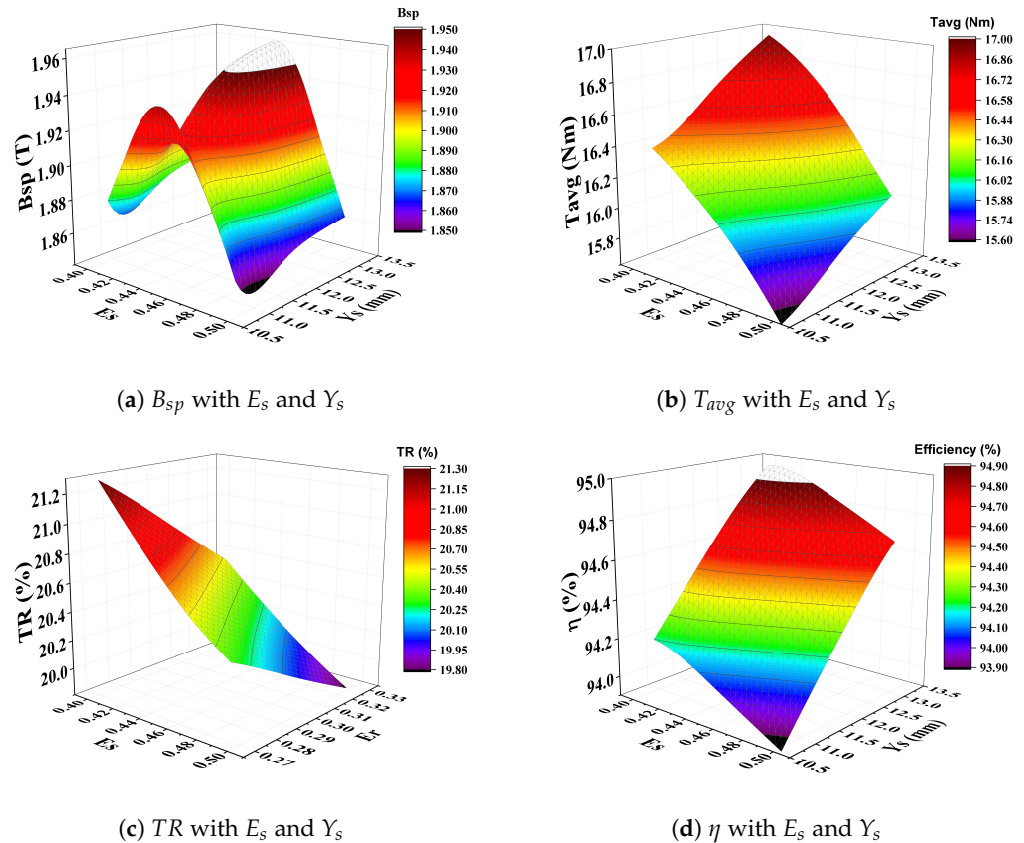(**d**) η with E_s and Y_s

Figure 11. 3D Response surface plots of the SRM. The plots display three-dimensional relationship between the parameters and are useful for establishing desirable response values.

Table 4. Details of Min–Max Search Algorithm.

Parameters	Y_s (mm)	E_s	E_r	η (%)	TR (%)	T_{avg} (Nm)	B_{sp} (T)
Minimum Values							
η (%)	10.80	0.50	0.33	**93.69**	19.83	15.30	1.86
TR (%)	13.20	0.50	0.33	94.52	**19.74**	15.79	1.87
T_{avg} (Nm)	10.80	0.50	0.33	93.69	19.83	**15.30**	1.86
B_{sp} (T)	11.08	0.50	0.28	94.08	20.35	15.58	**1.83**
Maximum Values							
η (%)	13.20	0.41	0.28	**94.99**	21.02	16.81	1.90
TR (%)	10.89	0.41	0.27	94.27	**21.35**	16.21	1.86
T_{avg} (Nm)	13.20	0.41	0.31	94.92	20.70	**17.00**	1.89
B_{sp} (T)	13.20	0.45	0.33	94.75	20.13	16.51	**1.97**

From Figure 11, the RS of the SRM were plotted based on the sensitivities of each of the design variables to the motor responses based on Figure 9. The Min-Max search algorithm was used to evaluate the response values of all the variables by searching the minima and maxima of each of the output parameters with their corresponding input parameters as listed in Table 4. The values were considered in the optimization program to obtain optimal solutions.

The multi-objective optimization problem can be stated as [41]:

$$
\begin{cases}
Maximize \ \overrightarrow{F}(\overrightarrow{x}) \\
\qquad\qquad subject\ to: \overrightarrow{g}(\overrightarrow{x}) \leq 0 \ and \ \overrightarrow{h}(\overrightarrow{x}) = 0. \\
\overrightarrow{X} = x_1, x_2, ..., x_n
\end{cases}
\tag{39}
$$

The vector $\overrightarrow{F}(\overrightarrow{X})$ includes several objective functions. It is defined as:
Objective:

$$
\min x(-T_{avg}(x), -\eta(x), TR(x)),
\tag{40}
$$

subject to: $X_L \leq x \leq X_u$; $\eta > 85\%$; $B_{sp} \leq B_{st}$,

where $x = (E_s, Y_s, E_r)$; $X_L = (0.41, 10.80, 0.27)$; $X_u = (0.50, 13.20, 0.33)$, B_{st} = saturating flux density which ranges from 1.7 T to 2.2 T depending on the steel material [43]. It is chosen as 1.8 6 T which is the knee point of the steel material.

The maximum and minimum limits of the variables in Table 2 were selected to give logical values with related physical meanings. These ranges were based on the power level (1.5 kW) of the motor. They were further checked to satisfy the following constraints:

$$
D_{sh} + 2b_{ry} + 2h_r + 2g = D,
\tag{41}
$$

$$
D + 2b_{sy} + 2h_s = D_0,
\tag{42}
$$

$$
\frac{E_s}{P_s} < \frac{E_r}{P_r},
\tag{43}
$$

$$
\frac{E_s}{P_s} + \frac{E_r}{P_r} < \frac{1}{P_r},
\tag{44}
$$

where b_{ry}, b_{sy}, E_s, and E_r are back iron lengths of rotor and stator, pole embraces of stator and rotor, respectively. E_s and E_r are given as:

$$
E_s < \frac{\beta_s * P_s}{2\pi},
\tag{45}
$$

$$
E_r < \frac{\beta_r * P_r}{2\pi}.
\tag{46}
$$

4. Results

4.1. Optimization Results

The NSGA-II algorithm is configured for 10,000 estimated evaluations with 500 samples every iteration and 500 initial samples for the solution of this study. The maximum number of candidates is three, and the permitted Pareto percentage is 70. Figure 12 and Figure 13 show the search direction of the objective functions with B_{sp} as more generations are produced at the set target of flux density of 1.86 T. The results show that a wide range of design solutions are found, offering significant improvements in weight and losses over the benchmark design.

A general criticism of optimization-based designs is that it is easy to lose track of the optimization process and, hence, useful engineering insights will not be gained from the design [52]. For improved clarity and visibility, three categories of plots are presented to visualize the process and observe design trends. The first category is the design variable plot in Figure 12, showing the input variables for the Pareto front solutions normalized to the upper and lower limits of their search space as displayed in Table 2. The second category is the output variables plot in Figure 13, showing the constrained performance outputs for the Pareto front solutions. The tradeoff plots between the output variables belong to the third category as shown in Figure 14. The optimization program was initiated to select three best candidate points among the generated solutions.
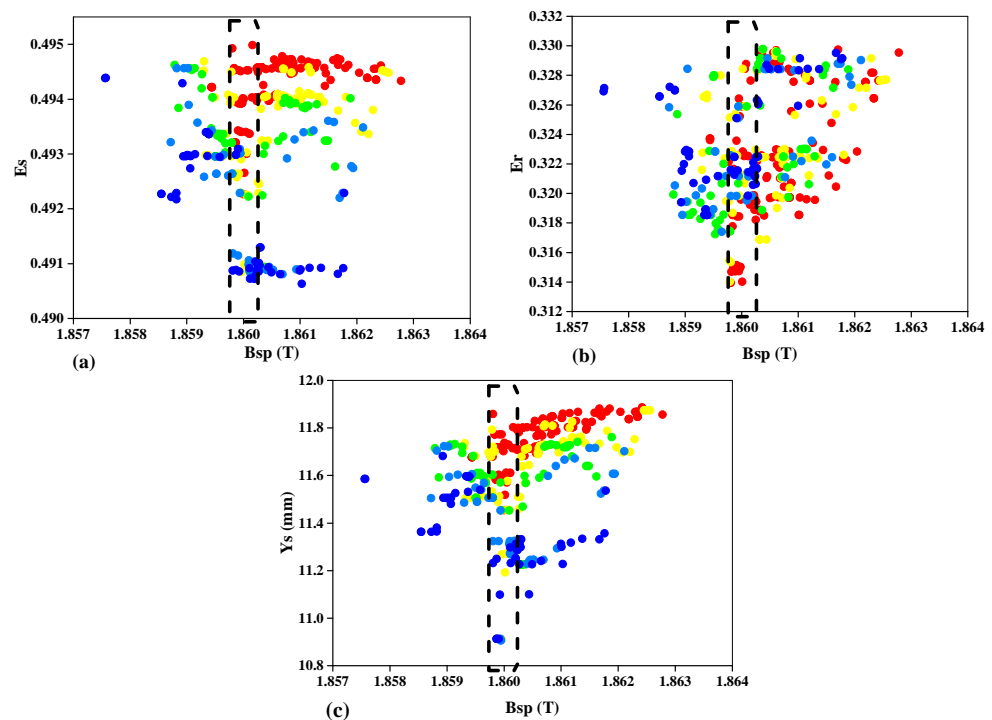
Figure 12. Tradeoff plot of input variables with B_{sp} (**a**) E_s with B_{sp} (**b**) E_r with B_{sp} (**c**) Y_s with B_{sp}. The input solutions highlighted in the dashed-line box dominate other solutions in the white areas since they are generated around 1.86 T. The best to worst solutions go from red to blue.

Figures 12 and 13 show that both the NSGA-II and GARS algorithms were able to find more feasible solutions for the target value of 1.86 T, but many of the obtained solutions fell outside the range of the optimal solutions meaning they were unfeasible. In each case, the solutions highlighted in the dashed-line box dominate other solutions in the white areas since they are generated around 1.86 T. The tradeoff plots represent the points at which improvement in one parameter's goal can be achieved without sacrificing the other at 1.86 T. Four Pareto fronts were obtained in the optimization process by solving (40), and the best to worst solution go from red to blue, respectively.
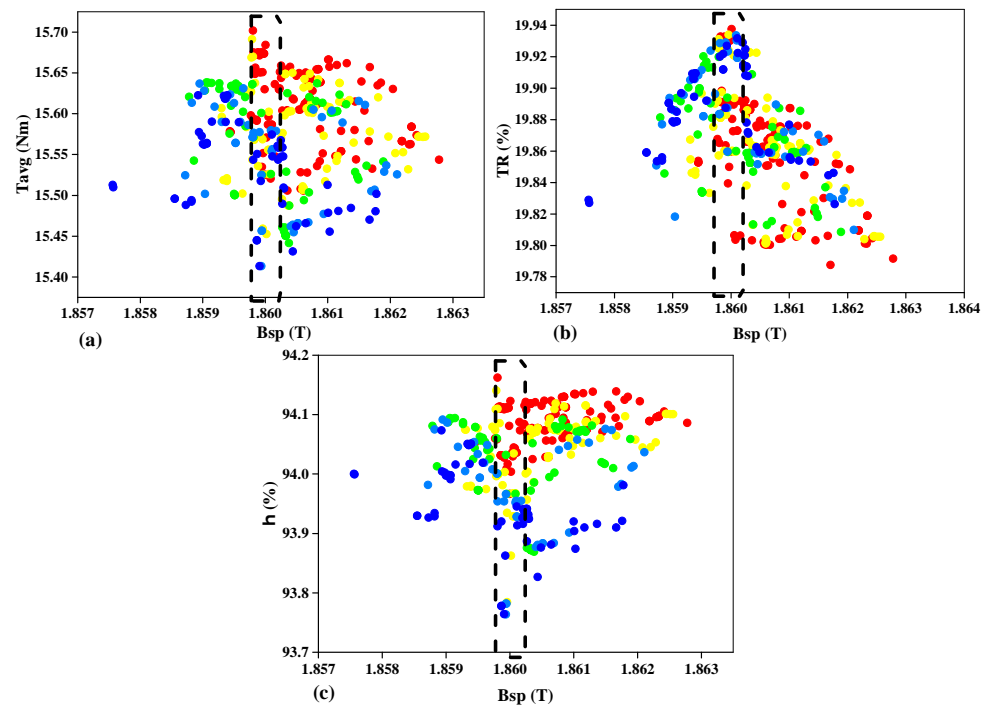
Figure 13. Tradeoff plot of output variables with B_{sp} (**a**) T_{avg} with B_{sp} (**b**) TR with B_{sp} (**c**) η with B_{sp}. The output solutions highlighted in the dashed-line box dominate other solutions in the white areas since they are generated around 1.86 T. The best to worst solutions go from red to blue.

From Figure 12a,b, a clear trend of increasing pole embraces of stator and rotor are observed for the target value of 1.86 T. The range of values for pole embraces of stator and rotor are between 0.492–0.495 and 0.326–0.328, respectively. These optimized values mean that the proposed model will bear sufficient pole overlap which will ensure enough torque during phase commutation. The best pole embrace arrangement will be chosen for the optimized model in order to minimise torque ripple because of its direct impact on inductance and torque calculation. Nevertheless, the range of values for stator yoke thickness is 11.45–11.73 mm which are lower than the benchmark value of 12 mm as seen in Figure 12c. This implies that the optimized model will have lower copper loss than the initial model because a wider stator pole causes more copper loss in electrical machines.

Furthermore, the relationship between motor responses and B_{sp} can also be seen in Figure 13. For B_{sp} of 1.86 T, the range of optimized values for torque, torque ripple and efficiency are 15.53–15.54 Nm (in Figure 13a), 19.81–19.86% (in Figure 13b), and 93.97–94.05% (in Figure 13c), respectively. The average torque is reduced to decrease the torque ripple, but at the same time, efficiency is increased, to ensure that the optimization objectives are not violated.

Figure 14 shows the relationships between the objective functions in pairs of (max, max), (max, min), and (min, max), respectively.

The candidate points denoted as Candidate A, Candidate B, and Candidate C in the plots represent the best designs that were generated by the optimization program. In this work, efficiency has most priority, followed by torque ripple and average torque. Therefore, the final selected candidate will have improved efficiency.

Since the objective is to optimize efficiency, average torque and torque ripple at 1.86 T, the program tries to achieve better candidates by searching right or left of the search area. It is obvious that the area which indicates the optimal search exists in either lower right and left quarter (considering the axes limits), where best values for efficiency, average torque, and torque ripples are sought. The best solutions for the (Max, Min) and (Min, Max) functions as seen in Figure 14b,c are in the lower left and right quarter, while the

best solutions of the (Max, Max) function of Figure 14a has a different shape because of the complexity of setting the program at 1.86 *T*.
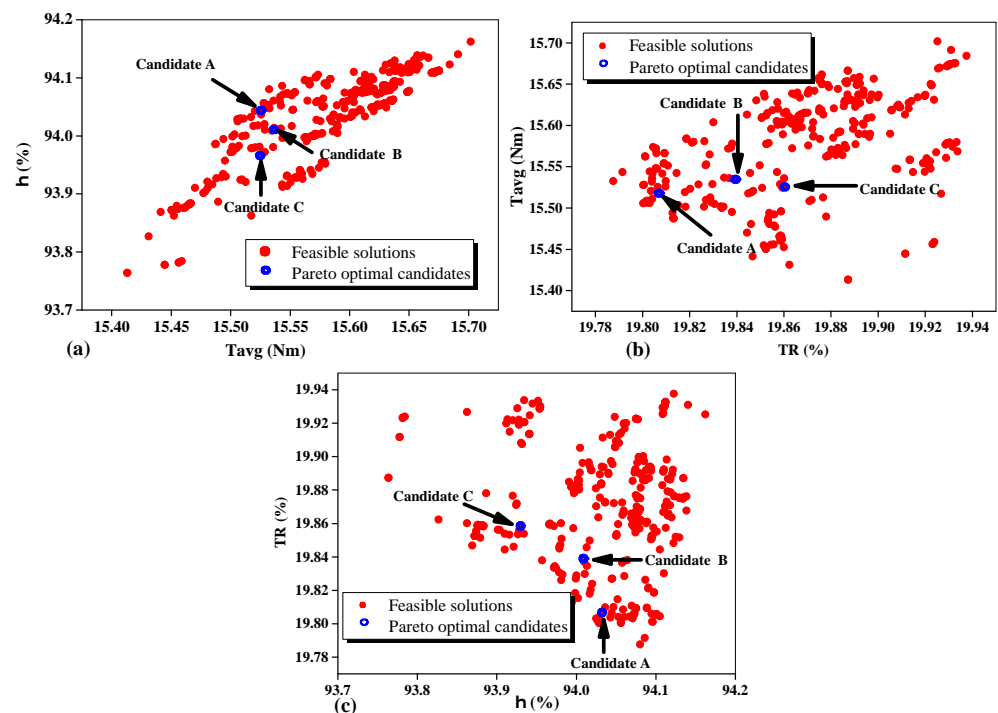
Figure 14. Pareto fronts of the multiobjective optimization obtained from the proposed GARS and NSGA-II-based method (**a**) Efficiency with Average Torque (**b**) Average Torque with Torque Ripple (**c**) Torque Ripple with Efficiency.

The input and output parameters of the initial model and the final candidates with their corresponding performance are specified in Table 5.

**Table 5.** Parameters of the initial model and optimal candidates at rated conditions .

Parameters	Initial Model	Candidate A	Candidate B	Candidate C
Y_s (mm)	12	11.73	11.59	11.45
E_s	0.45	0.50	0.49	0.49
E_r	0.30	0.33	0.33	0.33
B_{sp} (T)	1.95	1.86	1.86	1.86
TR (%)	20.41	19.81	19.84	19.86
T_{avg} (Nm)	16.32	15.53	15.54	15.53
Efficiency (%)	85	94.05	94.01	93.97

Table 5 shows the candidates of final generation with the three objective functions. The results shown confirm the accuracy of the search direction and proposed method.

4.2. Finite Element Verification of the Optimized Model

This section validates the pareto optimum candidate produced by the proposed approach and further assesses its efficacy using time-stepping finite element analysis. One of the most crucial and effective tools for this is the finite element analysis-based Maxwell software. A 2D finite element simulation of Candidate A (in Table 5) was performed using the software.

Figure 15 shows finite element mesh of the optimized motor. Mesh engineering was performed, and the finite element mesh was constructed with surface approximation of 0.065 mm and normal deviation of 15^0 and 12,407 surface elements. The meshing comprises of various mesh types in the model's different regions (stator, core, and coils).
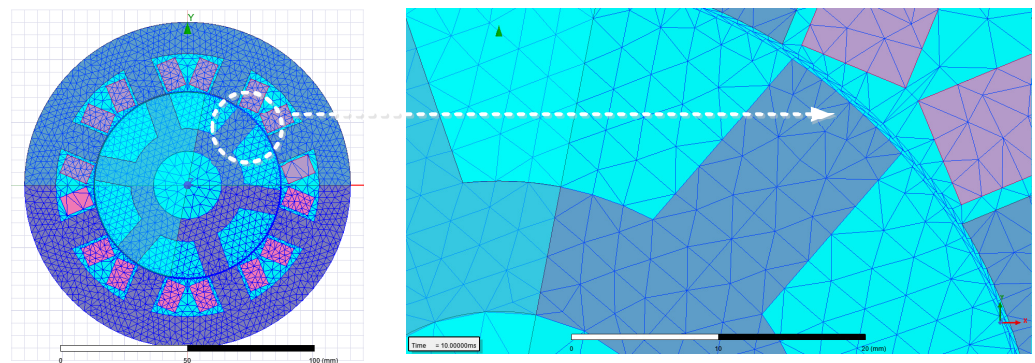
Figure 15. Meshing of the optimized model. A zoomed-in view is also provided for improved mesh detail.

The comparative characteristics of the initial and optimized models are shown in Figure 16. The equivalent flux linkages of the initial and optimized models were observed to be 0.463 Wb and 0.358 Wb, respectively as shown in Figure 16a. The 22.68% decrease in the flux linkages noticed in the optimized model means a reduction in energy conversion per each step which shows that magnetization will occur slower than the initial model. This led to reduction in torque production as compared with the initial model.
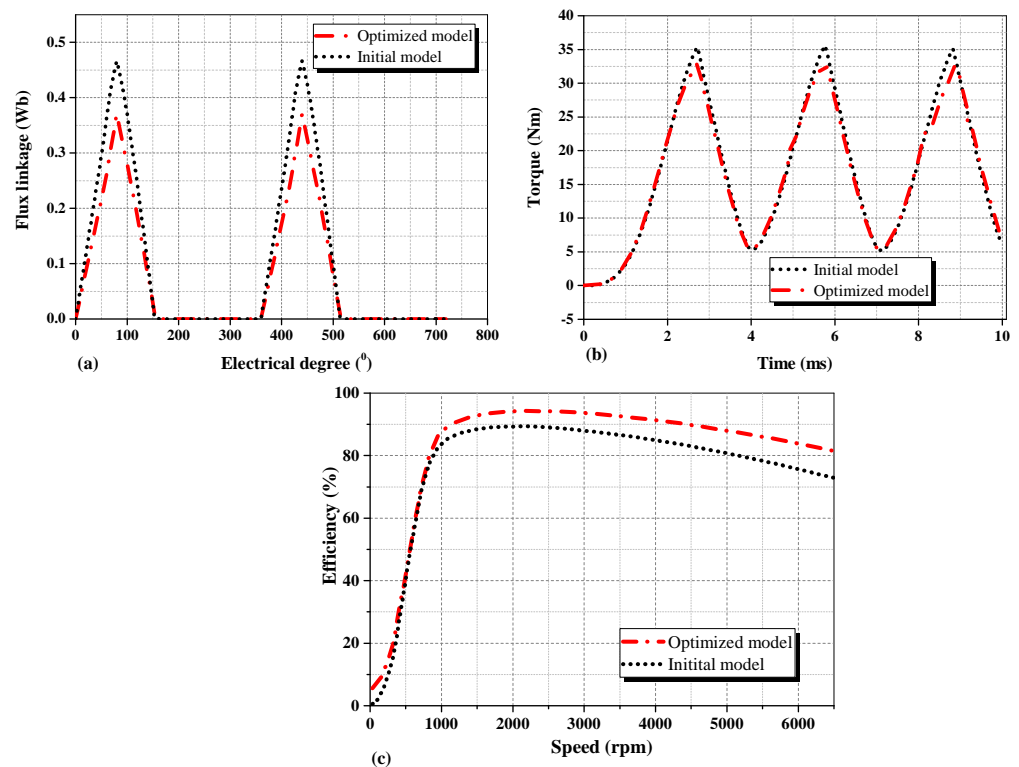
Figure 16. Comparison of motor performance of the initial and optimized model (**a**) Flux linkage characteristics (**b**) Torque profile (**c**) Motor efficiency with speed.

In Figure 16b, the output torque of the initial model (36.08 Nm) is higher than that of the optimized model (32.55 Nm) due to the higher flux linkages of the initial model. Nevertheless, torque ripple of the optimized model is lower than the initial model as a result of the influence of the optimized parameters that were used in the design of the optimized SRM model. The ripples were evaluated with the FEM tool used in this paper based on Equation (28).

Figure 16c shows the efficiency profile of the initial and optimized motor. It could be observed that the values of efficiency of both models are almost identical with each other until the speed reached 900 rpm. In addition, the optimized SRM recorded better efficiency response than the initial SRM over a wide speed range. The maximum efficiencies of initial and optimized models are 85% and 94.045%, respectively, at 2000 rpm, which shows the additional capabilities of the proposed optimizing process.

From Figure 16, it is apparent that there is significant improvement in the characteristics of the optimized model when compared with the initial model. The proposed techniques in [24,53] are general, however, they made a lot of assumptions and use mathematical models in the analysis to reduce computational time, which makes the process more complex and needs more analytical work before the commencement of the optimization process. Efficiency values are 75–80%, 80–86%, 82–85%, 80–85% and 73.83–88.18% in [24,25,54–56], respectively, while efficiency values of 93.97–94.05% are achieved for the three Pareto optimal candidates in this study. The approach proposed in this paper has shown success in optimization, as objective function values indicate. In addition, it can be adopted for any electrical machine optimization if the suitable objective functions and constraints are added.

5. Conclusions

This paper offered a thorough framework for SRM design optimization utilising GARS and MOGA while taking into account the objectives of average torque, efficiency, and torque ripple. FEA analysis is adopted in the optimization process as it provides high accuracy. The maximum flux density in the motor was limited to 1.86 *T* which is the knee point of the industrial steel used as the core material. GARS was proposed to find important design factors to build RS models for the ensuing optimization, while NSGA-II was used because of its excellent performance and intensification in optimization issues.

The results show the variation of variables that were considered in the optimization of the objective functions. The equivalent maximum flux linkages of the initial and optimized models were observed to be 0.463 Wb and 0.358 Wb, respectively. The 22.68% decrease in the flux linkages of the optimized model led to its reduced torque production. Nevertheless, torque ripple of the optimized model was lower than that of the initial model as a result of the influence of the optimized parameters that were used in the design of the optimized model.

Furthermore, the optimized SRM exhibits a better efficiency profile than the initial SRM over a wide speed range. The initial and optimized models recorded maximum efficiencies of 85% and 94.045%, respectively, at 2000 rpm. The efficiency values of 93.97–94.05% were achieved for the three Pareto optimal candidates in this study which are better the values obtained in related literature. This proves the success of the proposed framework for performance improvement of SRM. However, further work is recommended before the framework is used to address the minimization of noise/vibration and for specific industrial applications.

Author Contributions: Conceptualization, C.E.A., O.I.O. and S.S.A.; methodology, C.E.A.; software, C.E.A.; validation, C.E.A.; formal analysis, C.E.A.; investigation, C.E.A.; resources, O.I.O. and S.S.A.; data curation, C.E.A.; writing—original draft preparation, C.E.A.; writing—review and editing, C.E.A., O.I.O. and S.S.A.; supervision, O.I.O. and S.S.A.; funding acquisition, O.I.O. and S.S.A. All authors have read and agreed to the published version of the manuscript.

Institutional Review Board Statement: Not applicable.

Informed Consent Statement: Not applicable.

Data Availability Statement: Not applicable.

Conflicts of Interest: The authors declare no conflict of interest.

References

1. Agamloh, E.; Von Jouanne, A.; Yokochi, A. An overview of electric machine trends in modern electric vehicles. *Machines* **2020**, *8*, 20. [CrossRef]
2. El-Refaie, A.; Osama, M. High specific power electrical machines: A system perspective. *CES Trans. Electr. Mach. Syst.* **2019**, *3*, 88–93. [CrossRef]
3. Ferreira, F.J.; Fong, J.A.; de Almeida, A.T. Ecoanalysis of variable-speed drives for flow regulation in pumping systems. *IEEE Trans. Ind. Electron.* **2010**, *58*, 2117–2125. [CrossRef]
4. Hwang, K.Y.; Rhee, S.B.; Yang, B.Y.; Kwon, B.I. Rotor pole design in spoke-type brushless DC motor by response surface method. *IEEE Trans. Magn.* **2007**, *43*, 1833–1836. [CrossRef]
5. Heron, C. Installing, Operating, and Maintaining dc Motors in a Paper Mill Environment: Using Proactive Measures That Promote Longevity. *IEEE Ind. Appl. Mag.* **2019**, *25*, 25–33. [CrossRef]
6. Zhu, Z.; Hu, J. Electrical machines and power-electronic systems for high-power wind energy generation applications: Part II–power electronics and control systems. *COMPEL Int. J. Comput. Math. Electr. Electron. Eng.* **2013**, *32*, 34–71. [CrossRef]
7. Chiba, A.; Takano, Y.; Takeno, M.; Imakawa, T.; Hoshi, N.; Takemoto, M.; Ogasawara, S. Torque density and efficiency improvements of a switched reluctance motor without rare-earth material for hybrid vehicles. *IEEE Trans. Ind. Appl.* **2011**, *47*, 1240–1246. [CrossRef]
8. Pang, D.C.; Wang, C.T. A wireless-driven, micro, axial-flux, single-phase switched reluctance motor. *Energies* **2018**, *11*, 2772. [CrossRef]
9. Abdalmagid, M.; Sayed, E.; Bakr, M.; Emadi, A. Geometry and Topology Optimization of Switched Reluctance Machines: A Review. *IEEE Access* **2022**, *10*, 5141–5170. [CrossRef]
10. Asgar, M.; Afjei, E.; Torkaman, H. A new strategy for design and analysis of a double-stator switched reluctance motor: Electromagnetics, FEM, and experiment. *IEEE Trans. Magn.* **2015**, *51*, 1–8. [CrossRef]
11. Li, S.; Zhang, S.; Habetler, T.G.; Harley, R.G. Modeling, design optimization, and applications of switched reluctance machines—A review. *IEEE Trans. Ind. Appl.* **2019**, *55*, 2660–2681. [CrossRef]
12. Nie, R.; Chen, H.; Liu, J.; Zhao, W.; Wang, X.; Palka, R. Compensation analysis of longitudinal end effect in three-phase switched-reluctance linear machines. *IET Electr. Power Appl.* **2020**, *14*, 165–174. [CrossRef]
13. Echenique, E.; Dixon, J.; Cárdenas, R.; Peña, R. Sensorless control for a switched reluctance wind generator, based on current slopes and neural networks. *IEEE Trans. Ind. Electron.* **2008**, *56*, 817–825. [CrossRef]
14. Chen, H.; Gu, J.J. Implementation of the three-phase switched reluctance machine system for motors and generators. *IEEE/ASME Trans. Mech.* **2009**, *15*, 421–432. [CrossRef]
15. Wang, X.; Palka, R.; Wardach, M. Nonlinear Digital Simulation Models of Switched Reluctance Motor Drive. *Energies* **2020**, *13*, 6715. [CrossRef]
16. May, H.; Canders, W.; Palka, R.; Holub, M. Optimisation of the feeding of switched reluctance machines for high speed and high power applications. *Stud. Appl. Electromagn. Mech* **2002**, *22*, 489–494.
17. Yan, W.; Chen, H.; Liu, X.; Ma, X.; Lv, Z.; Wang, X.; Palka, R.; Chen, L.; Wang, K. Design and multi-objective optimisation of SRM with iron loss. *IET Electr. Power Appl.* **2019**, *13*, 435–444. [CrossRef]
18. Krishnan, R.; Blanding, D.; Bhanot, A.; Staley, A.; Lobo, N. High reliability SRM drive system for aerospace applications. In Proceedings of the 29th Annual Conference of the IEEE Industrial Electronics Society (IEEE Cat. No. 03CH37468) (IECON'03), Roanoke, VA, USA, 2–6 November 2003; Volume 2, pp. 1110–1115. [CrossRef]
19. Chang, Y.C.; Liaw, C.M. On the design of power circuit and control scheme for switched reluctance generator. *IEEE Trans. Power Electron.* **2008**, *23*, 445–454. [CrossRef]
20. Han, S.; Liu, C.; Sun, X.; Diao, K.; Wu, J. Investigation of static characteristics in six-phase switched reluctance motors under different winding connections. *IEEE Access* **2019**, *7*, 71174–71184. [CrossRef]
21. Krishnamurthy, M.; Edrington, C.S.; Emadi, A.; Asadi, P.; Ehsani, M.; Fahimi, B. Making the case for applications of SRM technology in automotive products. *IEEE Trans. Power Electron.* **2006**, *21*, 659–675. [CrossRef]
22. Du, L.; Gu, B.; Lai, J.S.J.; Swint, E. Control of pseudo-sinusoidal switched reluctance motor with zero torque ripple and reduced input current ripple. In Proceedings of the 2013 IEEE Energy Conversion Congress and Exposition, Denver, CO, USA, 15–19 September 2013; pp. 3770–3775. [CrossRef]
23. Gan, C.; Wu, J.; Sun, Q.; Kong, W.; Li, H.; Hu, Y. A review on machine topologies and control techniques for low-noise switched reluctance motors in EV applications. *IEEE Access* **2018**, *6*, 31430–31443. [CrossRef]
24. Ma, C.; Qu, L. Multiobjective optimization of switched reluctance motors based on design of experiments and particle swarm optimization. *IEEE Trans. Energy Convers.* **2015**, *30*, 1144–1153. [CrossRef]

25. El-Nemr, M.; Afifi, M.; Rezk, H.; Ibrahim, M. Finite element based overall optimization of switched reluctance motor using multi-objective genetic algorithm (NSGA-II). *Mathematics* **2021**, *9*, 576. [CrossRef]
26. Zhang, J.; Wang, H.; Chen, L.; Tan, C.; Wang, Y. Multi-objective optimal design of bearingless SRM based on multi-objective genetic particle swarm optimizer. *IEEE Trans. Magn.* **2017**, *54*, 1–13. [CrossRef]
27. Kocan, S.; Rafajdus, P.; Bastovansky, R.; Lenhard, R.; Stano, M. Design and Optimization of a High-Speed Switched Reluctance Motor. *Energies* **2021**, *14*, 6733. [CrossRef]
28. Ma, C.; Qu, L. Design considerations of switched reluctance motors with bipolar excitation for low torque ripple applications. In Proceedings of the 2013 IEEE Energy Conversion Congress and Exposition, Denver, CO, USA, 15–19 September 2013; pp. 926–933. [CrossRef]
29. Hu, Y.; Ding, W.; Wang, T.; Li, S.; Yang, S.; Yin, Z. Investigation on a multimode switched reluctance motor: Design, optimization, electromagnetic analysis, and experiment. *IEEE Trans. Ind. Electron.* **2017**, *64*, 9886–9895. [CrossRef]
30. Zhang, J.; Wang, H.; Zhu, S.; Lu, T. Multi-physics multi-objective optimal design of bearingless switched reluctance motor based on finite-element method. *Energies* **2019**, *12*, 2374. [CrossRef]
31. Rahman, M.S.; Lukman, G.F.; Hieu, P.T.; Jeong, K.I.; Ahn, J.W. Optimization and Characteristics Analysis of High Torque Density 12/8 Switched Reluctance Motor Using Metaheuristic Gray Wolf Optimization Algorithm. *Energies* **2021**, *14*, 2013. [CrossRef]
32. Song, S.; Fang, G.; Hei, R.; Jiang, J.; Ma, R.; Liu, W. Torque ripple and efficiency online optimization of switched reluctance machine based on torque per ampere characteristics. *IEEE Trans. Power Electron.* **2020**, *35*, 9608–9616. [CrossRef]
33. Xue, X.; Cheng, K.W.E.; Ng, T.W.; Cheung, N.C. Multi-objective optimization design of in-wheel switched reluctance motors in electric vehicles. *IEEE Trans. Ind. Electron.* **2010**, *57*, 2980–2987. [CrossRef]
34. Lan, Y.; Benomar, Y.; Deepak, K.; Aksoz, A.; Baghdadi, M.E.; Bostanci, E.; Hegazy, O. Switched reluctance motors and drive systems for electric vehicle powertrains: State of the art analysis and future trends. *Energies* **2021**, *14*, 2079. [CrossRef]
35. Zhang, P.; Ionel, D.M.; Demerdash, N.A. Morphing parametric modeling and design optimization of spoke and V-type permanent magnet machines by combined design of experiments and differential evolution algorithms. In Proceedings of the 2013 IEEE Energy Conversion Congress and Exposition, Denver, CO, USA, 15–19 September 2013; pp. 5056–5063. [CrossRef]
36. Gaing, Z.L.; Lin, C.H.; Tsai, M.H.; Hsieh, M.F.; Tsai, M.C. Rigorous design and optimization of brushless PM motor using response surface methodology with quantum-behaved PSO operator. *IEEE Trans. Magn.* **2013**, *50*, 1–4. [CrossRef]
37. Balaji, M.; Kamaraj, V. Evolutionary computation based multi-objective pole shape optimization of switched reluctance machine. *Int. J. Electr. Power Energy Syst.* **2012**, *43*, 63–69. [CrossRef]
38. Sahin, F.; Ertan, H.B.; Leblebicioglu, K. Optimum geometry for torque ripple minimization of switched reluctance motors. *IEEE Trans. Energy Convers.* **2000**, *15*, 30–39. [CrossRef]
39. Miller, T. Optimal design of switched reluctance motors. *IEEE Trans. Ind. Electron.* **2002**, *49*, 15–27. [CrossRef]
40. Husain, I. Minimization of torque ripple in SRM drives. *IEEE Trans. Ind. Electron.* **2002**, *49*, 28–39. [CrossRef]
41. Abunike, E.C.; Okoro, O.I.; Davidson, I.E. Finite Element Design and Multi-objective Optimization of Four Pole Reluctance Motor Based on NSGA-II Intelligent Algorithm. In Proceedings of the 2021 IEEE AFRICON, Arusha, Tanzania, 13–15 September 2021; pp. 1–6. [CrossRef]
42. Krishnan, R. *Switched Reluctance Motor Drives: Modeling, Simulation, Analysis, Design, and Applications*; CRC Press: Boca Raton, FL, USA, 2017. [CrossRef]
43. Vijayraghavan, P. Design of Switched Reluctance Motors and Development of a Universal Controller for Switched Reluctance and Permanent Magnet Brushless DC Motor Drives. Ph.D. Thesis, Virginia Polytechnic Institute and State University, Blacksburg, VA, USA, 2001.
44. Ibrahim, M.N.F.; Sergeant, P. Prediction of eddy current losses in cooling tubes of direct cooled windings in electric machines. *Mathematics* **2019**, *7*, 1096. [CrossRef]
45. Abunike, E.C.; Okoro, O.I.; Davidson, I.E. Thermal Analysis of an Optimized Switched Reluctance Motor for Enhanced Performance. In Proceedings of the 2021 IEEE PES/IAS PowerAfrica, Virtual, 27 August 2021; pp. 1–5. [CrossRef]
46. Hayashi, Y.; Miller, T.J. A new approach to calculating core losses in the SRM. *IEEE Trans. Ind. Appl.* **1995**, *31*, 1039–1046. [CrossRef]
47. Ilka, R.; Alinejad-Beromi, Y.; Yaghobi, H. Cogging torque reduction of permanent magnet synchronous motor using multi-objective optimization. *Math. Comput. Simul.* **2018**, *153*, 83–95. [CrossRef]
48. Deb, K.; Pratap, A.; Agarwal, S.; Meyarivan, T. A fast and elitist multiobjective genetic algorithm: NSGA-II. *IEEE Trans. Evol. Comput.* **2002**, *6*, 182–197. [CrossRef]
49. Song, X.; Park, Y.; Li, J.; Lee, J. Optimization of switched reluctance motor for efficiency improvement using response surface model and kriging model. In Proceedings of the IEEE 2011 Fourth International Joint Conference on Computational Sciences and Optimization, Kunming and Lijiang, China, 15–19 April 2011; pp. 259–260. [CrossRef]
50. Acar, E. Various approaches for constructing an ensemble of metamodels using local measures. *Struct. Multidiscip. Optim.* **2010**, *42*, 879–896. [CrossRef]
51. Rousson, V.; Goşoniu, N.F. An R-square coefficient based on final prediction error. *Stat. Methodol.* **2007**, *4*, 331–340. [CrossRef]
52. Cheong, B.; Giangrande, P.; Zhang, X.; Galea, M.; Zanchetta, P.; Wheeler, P. Evolutionary multiobjective optimization of a system-level motor drive design. *IEEE Trans. Ind. Appli.* **2020**, *56*, 6904–6913. [CrossRef]

53. El-Wakeel, A.; Smith, A. Optimal design of switched reluctance motors using genetic algorithms. In Proceedings of the ICEM, Brugge, Belgium, 25–28 August 2002.

54. Li, S.; Zhang, S.; Jiang, C.; Mayor, J.R.; Habetler, T.G.; Harley, R.G. A fast control-integrated and multiphysics-based multi-objective design optimization of switched reluctance machines. In Proceedings of the 2017 IEEE Energy Conversion Congress and Exposition (ECCE), Cincinnati, OH, USA, 1–5 October 2017; pp. 730–737. [CrossRef]

55. Anvari, B.; Toliyat, H.A.; Fahimi, B. Simultaneous optimization of geometry and firing angles for in-wheel switched reluctance motor drive. *IEEE Trans. Transp. Electrif.* **2017**, *4*, 322–329. [CrossRef]

56. Yalavarthi, A.; Singh, B.; Modi, M.; Dudharejiya, D.; Jain, C. Design Optimization of Switched Reluctance Surface Motor using Finite Element Analysis. In Proceedings of the IEEE 2020 International Conference on Power, Instrumentation, Control and Computing (PICC), Thrissur, India, 17–19 December 2020; pp. 1–6. [CrossRef]